INORGANIC CHEMISTRY FRONTIERS

RESEARCH ARTICLE

View Article Online
View Journal

Cite this: DOI: 10.1039/d5qi02257f

Vanadium thiocarboxylate metal–organic frameworks as efficient photocatalysts for photooxidative desulfurization

Pablo Salcedo-Abraira, *[a,b] Yolanda Pérez, *[c,d] Clara García-Abad,[c] Nathalie Guillou,[e] Patricia Horcajada [c] and Thomas Devic *[b]

Air pollution causes the premature death of *ca.* 7 million people each year, with SO_x gases being among the most harmful contaminants. Reducing the sulfur content in liquid fossil fuels is crucial for overcoming this health and environmental issue. Among the different available technologies, photooxidative desulfurization (PODS) stands out as one of the most promising methods, since it only requires sunlight to drive the reaction. Metal–Organic Frameworks (MOFs), with their tunable porosity and chemical diversity, have emerged as potential adsorbents and photocatalysts for the removal of sulfur-containing compounds from fuels. In this work, the reactivity of the ligand 2,5-disulfhydrylbenzene-1,4-dicarboxylic acid (H_4DSBDC) with different V salts was evaluated to prepare new photocatalytically active metal–organic frameworks. Two new compounds, labeled (DMA)$KV^{IV}O$(DSBDC) and MIL-47(V^{III})-$(SCH_3)_2$, were successfully synthesized *via* solvothermal methods. X-Ray diffraction structural analysis revealed that the second solid relies exclusively on V–O bonds, whereas both V–O and V–S bonds are found in the first one. Both MOFs are stable in suspension and absorb light in the visible region, prompting their evaluation as photocatalysts for visible-light-driven reactions. For the first time, V-based metal–organic frameworks are proposed for the photooxidative desulfurization reaction. Among them, MIL-47(V)-$(SCH_3)_2$ demonstrated superior performance, achieving a desulfurization efficiency of 73%, which was maintained for at least 4 consecutive cycles.

Received 6th November 2025,
Accepted 7th December 2025

DOI: 10.1039/d5qi02257f

rsc.li/frontiers-inorganic

Introduction

According to the World Health Organization (WHO), approximately 7 million premature deaths are caused each year due to exposure to air pollution,[1] recommending air quality levels for 6 key contaminants: nitrogen dioxide (NO_2), sulfur dioxide (SO_2), carbon monoxide (CO), ozone (O_3) and particulate matter (PM). In this context, the combustion of sulfur-containing compounds in conventional fossil fuels (*e.g.*, gasoline and diesel) releases harmful sulfur oxides (SO_x) into the atmosphere, which react with water and form acid rain. Therefore, reducing the sulfur content in liquid fuels is urgently required to mitigate the serious environmental and health issues caused by SO_2 emissions[2] and to comply with strict regulations (*i.e.*, 10–15 ppm of sulfur)[3] aimed at achieving ultra-low-sulfur fuel standards. To date, various methods have been developed to remove sulfur from fuels, including adsorptive desulfurization (ADS), biodesulfurization (BDS), oxidative desulfurization (ODS), extractive desulfurization (EDS) and hydrodesulfurization (HDS).[4] Among them, HDS is the most widely used technology. However, it requires harsh operating conditions (*i.e.*, H_2 pressure and temperature), incurs substantial costs, and is of limited efficiency for removing refractory sulfur compounds (*e.g.*, dibenzothiophene and DBT),[5] which must be eliminated to comply with applicable regulations. In contrast, visible-light photo-driven ODS (or PODS) has gained significant attention due to its mild operating conditions, low energy requirements (using sunlight), enhanced safety (no hydrogen involved) and environmentally friendly nature, demonstrating excellent efficiency in removing refractory sulfur compounds.[6] Visible-light-driven ODS involves two main steps: (i) oxidation

[a]*Department of Inorganic Chemistry, University of Granada, Avda. Fuente nueva s/n, 18071 Granada, Spain. E-mail: psalcedo@ugr.es*
[b]*Nantes Université, CNRS, Institut des Matériaux de Nantes Jean Rouxel, IMN, F-44000 Nantes, France. E-mail: thomas.devic@cnrs-imn.fr*
[c]*IMDEA Energy Institute, Advanced Porous Materials Unit (APMU), Avda. Ramón de la Sagra 3, E-28935 Móstoles, Madrid, Spain. E-mail: yolanda.cortes@urjc.es*
[d]*COMET-NANO Group, Departamento de Biología y Geología, Física y Química Inorgánica, ESCET, Universidad Rey Juan Carlos, C/Tulipán s/n, 28933 Móstoles, Madrid, Spain*
[e]*Institut Lavoisier de Versailles, UMR CNRS 8180, Université de Versailles St-Quentin en Yvelines, Université Paris Saclay, 78035 Versailles, France*

of sulfur-containing compounds into the corresponding sulfones by reactive oxygen species (ROS), generated from an oxidizing agent in the presence of a photocatalyst under visible light irradiation, followed by (ii) extraction of the resulting sulfones.

Despite the promising potential of PODS, the development of efficient and robust photocatalysts remains crucial for advancing sustainable and cost-efficient desulfurization technologies. In this scenario, Metal–Organic Frameworks (MOFs) appear as potential candidates due to their chemical diversity and their easily tunable properties, although they might suffer from insufficient chemical stability and fast electron–hole recombination. While composite materials where MOFs act as a host or a support of the active catalyst have been reported,[7–10] the use of pure MOFs for PODS has only been recently investigated. For instance, the zeolitic imidazolate framework ZIF-67[11] and the Zr-based MOF NH_2-UiO-66,[12] both of which possess wide optical band gaps (>3 eV), were found to be active for the photocatalytic degradation of dibenzothiophene (DBT) under visible light irradiation in the presence of H_2O_2 as an oxidant. The Ti-based MOF MIL-125-NH_2, with a narrower band gap of 2.32 eV, demonstrated superior photocatalytic performance in ODS, achieving 70% DBT removal within 25 min.[13] Inorganic vanadium-based materials (*e.g.*, V_2O_5–ZnO and Ag_3VO_4)[14,15] have also demonstrated promising photocatalytic activity for PODS, in line with the ability of V to adopt several oxidation states and favor electron transfer. Although V-based MOFs are considered as potential candidates for photocatalytic processes in environmental applications,[16] to the best of our knowledge, they have not yet been explored as photocatalysts for light-driven ODS, and their application in thermally driven ODS has been scarcely reported.[16] In the present work, we aimed to develop V-based MOFs with optimized optical absorption features and to evaluate their PODS activity. We selected the ligand 2,5-disulfhydrylbenzene-1,4-dicarboxylic acid (H_4DSBDC), which not only absorbs light in the visible range through π–π* transitions but also can give rise to additional absorption through ligand-to-metal charge transfer (LMCT) *via* M–S bonds. Although most MOFs based on DSBDC follow Pearson's hard and soft acid and base (HSAB) theory,[17] meaning that materials based on M^{I} or M^{II} cations are built through M–S and M–O bonds[18–22] and those based on M^{III} or M^{IV} are based exclusively on M–O bonds,[20,23–28] we recently showed that Fe^{III} and DSBDC can give rise to stable materials comprising M–S bonds.[29,30] With this in mind, we here evaluated the reactivity of the H_4DSBDC ligand with V^{III} and V^{IV} cations, leading to the successful synthesis of two new coordination polymers. The first solid, (DMA)KVO(DSBDC), presents coordination of V^{IV} to both O and S atoms, while the second is an analogue of MIL-47(V), denoted MIL-47(V)-$(SCH_3)_2$, hence comprising only M–O bonds. The thermal features, chemical stability and optical properties of these materials are here reported, as well as their photocatalytic activities for the oxidation of DBT.

Results and discussion

Synthesis and physicochemical characterization

H_4DSBDC was prepared on a multi-gram scale following the reported protocol.[31] Its reactivity with V salts was first systematically investigated using the high throughput solvothermal reactors developed by Stock *et al.*[32] The nature of the solvent (water, alcohols, *N*,*N*-dimethylformamide (DMF) and mixtures) and the vanadium precursors ($V^{III}Cl_3$, $V^{IV}OSO_4$, $V^{IV}O(acac)_2$) was investigated, as well as the effects of the time, temperature and the addition of acids (HCl, acetic acid (AcOH)) or bases (MOH, M = Li, Na, K). Two crystalline phases were identified, and their syntheses were further scaled up for full characterization. It is worth noting here that the yields of both syntheses (75% and 95%, respectively) are more than twice, with some exceptions,[33–35] the ones typically reported for V-based MOFs prepared under solvothermal conditions (<40%).[36–42]

The first solid was obtained from a mixture of VCl_3 and H_4DSBDC in DMF–water at 180 °C in the presence of KOH (yield ≈ 75% based on V). Interestingly, the base has a strong influence on the reaction output: only amorphous solids were obtained when using LiOH or NaOH instead of KOH, in line with the crystal structure (see below). Amorphous solids were also obtained upon the addition of extra base (4 or 6 equivalents instead of 2) or when using a mixture of solvents (*i.e.*, methanol and DMF) (Table S1). On the other hand, the vanadium precursor has only a minor influence on the result, since the same material can be obtained by using $V^{III}Cl_3$ or $V^{IV}O(acac)_2$, although in the latter case, smaller particle sizes and a mixture of phases were observed (Fig. S1). The micrometric size of the obtained crystals (~50 μm, Fig. S2) allowed the elucidation of the crystalline structure by using conventional single-crystal X-ray diffraction (SC-XRD). The material, formulated $(C_2H_8N)KVO(C_8H_2O_4S_2)$ and denoted (DMA)$KV^{IV}O$(DSBDC), crystallizes in the triclinic space group $P\bar{1}$ with a = 6.9416(5) Å, b = 10.3763(7) Å, c = 10.4436(7) Å, α = 101.025(6)°, β = 101.363(6)°, γ = 98.543(6)° and V = 710.19(9) Å^3 (Tables 1 and S2; CCDC 2246050). The structure consists of fully deprotonated $DSBDC^{4-}$ ligands (Fig. 1a) bound to vanadium and potassium to define an anionic network with entrapped di-

Table 1 Unit cell parameters of (DMA)KVO(DSBDC) and MIL-47(V)-$(SCH_3)_2$

Compound	(DMA)KVO(DSBDC)	MIL-47(V)-$(SCH_3)_2$
Chemical formula	$(C_2H_7N)KVO(C_8H_2S_2O_4)$	$VOH(C_{10}H_8S_2O_4)$
Crystal system	Triclinic	Monoclinic
Wavelength	0.71073 Å	0.671415 Å
Space group	$P\bar{1}$	$C2/c$
a	6.9416(5) Å	18.9190(4) Å
b	10.3763(7) Å	11.6119(3) Å
c	10.4436(7) Å	6.87187(2) Å
α	101.025(6)°	—
β	101.363(6)°	108.9768(1)°
γ	98.543(6)°	—
V	710.19(9) Å^3	1427.60(7) Å^3
M_{20}	—	87
Z	2	4

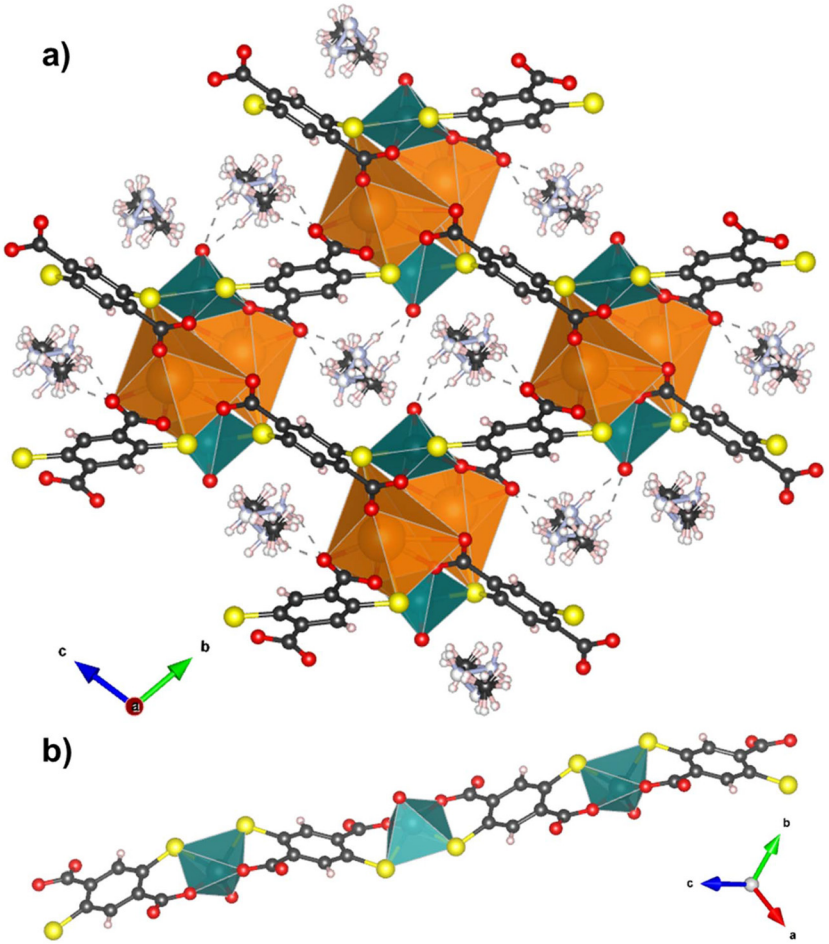

Fig. 1 Crystalline structure of (DMA)KVO(DSBDC): (a) view along the *a* axis and (b) representation of the VO(DSBDC) 1-D chain. Vanadium, potassium, sulfur, oxygen, nitrogen, carbon and hydrogen are represented in dark green, orange, yellow, red, pale blue, black and white, respectively.

methylammonium (DMA) cations. Note that the presence of such an organic cation can be easily rationalized considering the DMF decomposition, as already reported for other MOFs prepared under similar synthetic conditions.[43] The vanadium ions are connected to two DSBDC linkers by both O and S atoms through 6-membered chelate rings (Fig. 1b) that define the square base of a pyramid with the V ion at the center. The apical position is occupied by an O atom, giving rise to the coordination motif VO_3S_2. The V–O apical distance is significantly shorter than the equatorial ones (1.59 and ~1.95 Å, respectively), indicating the formation of a vanadyl V=O bond, which is characteristic of V^{IV} complexes.[44,45] The oxidation state of the vanadium is further confirmed by bond valence calculations (BVC, Table 2)[46] and charge balance consideration. The resulting anionic $\{VO(DSBDC)^{2-}\}_n$ chains further interact with K^+ cations (d_{K-O} = 2.61–3.2 Å; d_{K-S} ~ 3.31 Å, Fig. S4), resulting in a 3D network with 1D channels (~8 × 4 $Å^2$ considering the van der Waals radii of the atoms). The alkali ions are thus part of the hybrid framework; considering the ionic radii of Li, Na and K (0.9, 1.16 and 1.52 Å, respectively), this probably explains why the framework could not be obtained with the smaller alkali. DMA cations are disordered within the cavities, establishing N–H···O hydrogen bonds with the carboxylate and vanadyl moieties. Finally, the purity of the polycrystalline samples prepared from VCl_3 was assessed by Rietveld refinement (Fig. S7 and Table S4) and elemental analysis (see the SI for further details), both indicating the absence of any impurities.

Table 2 V–O and V–S bond distances and bond valence calculations for the obtained materials

Compound	Bond	Distance (Å)	Bond valence		*V* ox. state
(DMA)KVO(DSBDC)	V–O	1.955(4)	0.65	4.11	+4
	V–O	1.965(3)	0.60		
	V–O_{vandyl}	1.598(4)	1.44		
	V–S	2.3357(1)	0.74		
	V–S	2.3650(1)	0.68		
MIL-47(V)-$(SCH_3)_2$	V–O (×2)	1.936(4)	0.59	3.18	+3
	V–O (×2)	2.009(9)	0.48		
	V–O (×2)	1.991(8)	0.51		

The second phase was obtained by reacting the H_4DSBDC and $V^{III}Cl_3$ in a mixture of DMF and methanol (MeOH) at 180 °C for 50 h (yield = 95% based on V). Unlike the (DMA) KVO(DSBDC) material, this second phase cannot be obtained by using $V^{IV}O(acac)_2$ as a precursor. The DMF : MeOH solvent ratio was systematically varied from 9 : 1 to 5 : 5, and a ratio of 8 : 2 was found to be optimal (Table S1 and Fig. S6). The replacement of methanol with other alcohols (ethanol, isopropanol) led to unidentified or amorphous phases (Table S1). The solid was initially obtained in the form of small crystallites (~0.5 μm, Fig. S3); attempts were made to increase the size of the crystals, including the use of mineralizing agents (HF), modulators (AcOH), and increasing the metal concentration (from 0.05 to 0.2 M). This allowed growing larger needle-like crystals up to 10 μm (Fig. S3), but still too small for SC-XRD. The crystal structure was then elucidated by synchrotron powder X-ray diffraction (PXRD). The material crystallized in the monoclinic space group $C2/c$ with a = 18.9190(4) Å, b = 11.6119(3) Å, c = 6.87 187(2) Å, β = 108.9768(1)°, and V = 1427.60(7) Å^3 (Fig. S8 and Table S3; CCDC 2497420). This phase exhibits a porous structure similar to that of the well-established MOF MIL-47(V) (Fig. 2a),[36,47] where chains of VO_6 octahedra sharing vertexes (Fig. 2b and S5) are connected by terephthalate ligands, creating channels along the c axis with an approximate size of 8 × 5.5 Å (considering the van der Waals radii of the atoms) that contain disordered DMF molecules representing 27% of the unit cell volume according to PLATON calculations. BVC (Table 2) confirmed the oxidation

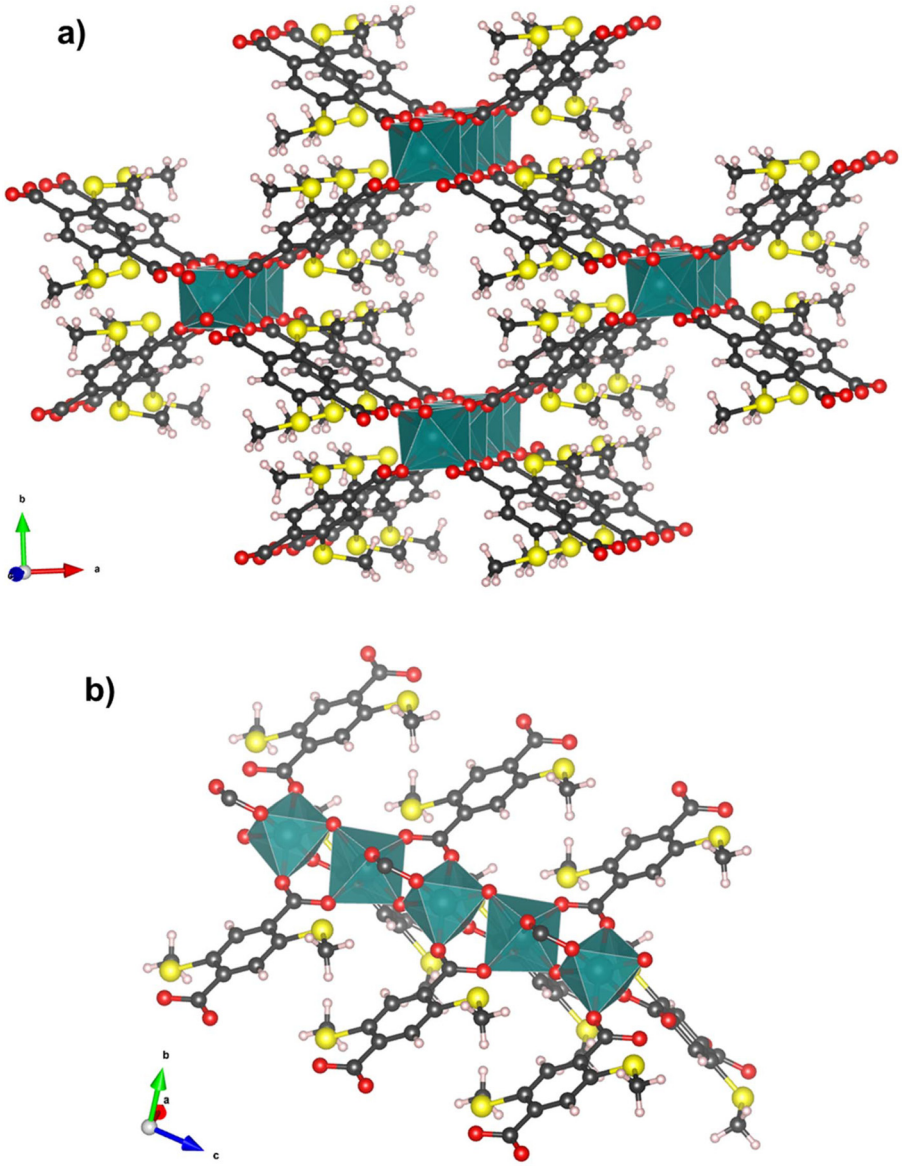

Fig. 2 Structure of MIL-47(V)-$(SCH_3)_2$ (a) and representation of the VO_6 chains (b). Vanadium, sulfur, oxygen, carbon and hydrogen are represented in dark green, yellow, red, black and white, respectively. Entrapped DMF molecules are omitted for the sake of clarity.

state of V as +III in the as-synthesized compound, similar to what is found in the non-functionalized MIL-47(V) material. The ligand is thus bound to the V^{III} ions through the O atoms only, but interestingly, the obtained material is not MIL-47(V)-$(SH)_2$, as could be expected when using the thiol-functionalized version of the terephthalate linker, but rather corresponds to the thiomethyl-functionalized version of the material (labeled MIL-47(V)-$(SCH_3)_2$), with the formula $V^{III}OH(Me_2DSBDC)\cdot$(guest) as confirmed by elemental analysis (see the SI). The linker methylation occurred through an irreversible *in situ* condensation reaction with methanol.

MIL-47(V)-$(SCH_3)_2$ is then exclusively built from V–O coordination bonds. In contrast, in the (DMA)KVO(DSBDC) material, both the carboxylate and thiolate groups are bound to the V^{IV} cation. Although this reactivity is not what is expected based on HSAB theory,[17] it agrees with the experimental observation in discrete coordination compounds, where the coordination of both hard (carboxylate) and soft (thiolate) groups of the linker to $M^{III/IV}$ cations was sometimes observed upon the addition of a base to the reaction medium.[48–51] This reactivity has also been recently reported by our group for a series of layered materials formulated as AFe(DSBDC) (A = Na, K, DMA), in which both S and O atoms from the DSBDC linker coordinate to the Fe^{III} center.[29] Interestingly, although the synthetic conditions are comparable and the coordination mode is identical (the metallic cation chelated through a 6-membered ring involving both the carboxylate and thiolate functions), the structures of the V- and Fe-based solids are markedly different. This can be easily explained considering the *in situ* oxidation of the V^{III} to create the VO^{2+} species, leading to isolated square-based VS_2O_3 pyramids instead of the FeS_4O_2 edge-sharing octahedra found in AFe(DSBDC).

These different coordination modes are in agreement with the Fourier transform infrared (FTIR) spectroscopy analysis. As can be seen in Fig. S12, when compared to the pristine ligand H_4DSBDC, one of the most significant differences is observed for the carboxylic/ate ν elongation bands in the 1700–1500 cm^{-1} region. For H_4DSBDC, a single band is observed at 1680 cm^{-1}, corresponding to the C═O bond. For (DMA)KVO(DSBDC), two bands are observed at lower wavenumbers (1616 and 1582 cm^{-1}), in line with the interaction of the carboxylate group with the V(IV) and K ions. For MIL-47(V)-$(SCH_3)_2$, a single band is found at a lower wavenumber (1541 cm^{-1}), as a consequence of the bonding to the V^{III} ions. This analysis supports the fact that the environments of the carboxylate moieties are very different in both MOFs. Another relevant difference is found for the ν C–S bands. In the spectra of both H_4DSBDC and (DMA)KVO(DSBDC), a single band appears at 634 and 627 cm^{-1}, respectively, and is attributed to the S–C_{arom} bond. In contrast, the spectrum of MIL-47(V)-$(SCH_3)_2$ exhibits two bands at 654 and 598 cm^{-1}, attributed to the S–C_{arom} and S–CH_3 bonds, confirming the alkylation of the S atoms during the synthesis. Additional attribution of the IR vibration bands can be found in Table S5.

The thermal stability of the materials was assessed by thermogravimetric analysis (TGA) and variable-temperature PXRD (VT-PXRD) under air, while the porosity was evaluated using N_2 sorption experiments at 77 K. For (DMA)KVO (DSBDC), no weight loss was detected on the TGA curve before 290 °C, in line with the absence of volatile species in the structure. Above this temperature, a continuous weight loss is observed up to 610 °C, and it is associated with the decomposition of the solid (Fig. S15). In good agreement with this, VT-PXRD experiments showed that the crystalline structure was maintained with no noticeable structural modification up to 280 °C, becoming amorphous at higher temperature when the decomposition started (Fig. S16). Both experiments confirmed the structural role of the DMA cations, which cannot be removed without compromising the structural integrity of the material. This was further confirmed by N_2 sorption experiments that evidenced no accessible porosity for this compound.

Two forms of MIL-47(V)-$(SCH_3)_2$ were studied: the pristine solid that contains DMF molecules in the pores (see above), and the MeOH-exchanged material. The latter was obtained by suspending the pristine material in MeOH (see the Experimental section for further information). IR spectroscopy confirmed the complete removal of the DMF molecules (Fig. S13), while the PXRD patterns and unit-cell parameters of both compounds present slight differences (Fig. S9), in line with the structural flexibility of MIL-47 materials (see below). The TGA curve of pristine MIL-47(V)-$(SCH_3)_2$ (Fig. S17) displayed an initial weight loss of around 10% from room temperature (RT) to 200 °C, which corresponds to DMF departure, followed by a second weight loss from 250 to 550 °C, attributed to material decomposition. The material suspended in MeOH presents a slightly different TGA curve (Fig. S19), with the decomposition occurring at 250 °C and solvent departure completed at 80 °C, in line with the lower boiling point of MeOH compared to DMF. In both cases, VT-PXRD data supported these findings, revealing an amorphization temperature for both solids of ~250 °C, associated with the degradation of the framework (Fig. S18 and S20). Below this temperature, a continuous shift of the diffraction peaks is observed whatever the initial pore content. Additional VT-PXRD experiments performed on the MeOH-exchanged sample showed that this behavior is reversible when the experiment is carried out under N_2 (Fig. S22), but not when performed under air (Fig. S21). These results can be rationalized in view of the behavior of MIL-47.[36,47] MIL-47 is formulated in its pristine state $V^{III}(OH)(BDC)\cdot$(guest). Similar to the isostructural MIL-53(M) (or M(OH)(BDC), M = Al, Cr, Fe, Ga) solid, this MOF presents high structural flexibility, associated with the existence of two extreme pore openings, the closed-pore (CP) and large-pore (LP) forms. When exposed to air at 200 °C, V^{III} is oxidized to V^{IV}, and the resulting solid, formulated as $V^{IV}O(BDC)$, becomes rigid whatever the adsorbate. In the present case, the shift of the diffraction peaks observed when heating MIL-47(V)-$(SCH_3)_2$ can be associated with structural flexibility, as expected for the reduced V^{III} form. Nevertheless, note that the shift is moderate, indicating a flexibility of lower amplitude than that of $V^{III}(OH)(BDC)\cdot$(guest). This phenomenon is

expected for MIL-53 type frameworks functionalized with bulky groups that prevent the complete breathing of the pore because of their steric hindrance.[52,53] The fact that this flexibility is not reversible when the experiment is carried out under air suggests at first sight an oxidation into $V^{IV}O$ (Me_2DSBDC) that becomes rigid, similar to $V^{IV}O$(BDC). Nevertheless, a partial degradation could also explain the irreversible diffraction peak broadening: the FTIR spectrum of the product after the thermal treatment (Fig. S14) indeed presents significant modification, including new bands at ~1170, 1230, ~1700 and ~3300 cm^{-1} possibly associated with $-SO_3H$ symmetric and asymmetric stretching, C═O and O–H vibrations, respectively, and the disappearance of the bands at ~2900 cm^{-1} and ~650 cm^{-1} associated with the $-SCH_3$ group, which suggests an irreversible oxidation of the organic ligand. The porosity of the MIL-47(V)-$(SCH_3)_2$ was confirmed experimentally by N_2 sorption on the MeOH-exchanged material. As expected, the solid presents a type I isotherm (Fig. S10), with S_{BET} = 450 m^2 g^{-1} and V_p = 0.18 cm^2 g^{-1}. Horvath–Kawazoe pore size distribution (Fig. S11) showed a pore diameter around 6 Å, which fairly agrees with the crystallographic pore size (8 × 5.5 Å, see above). The minor difference could be rationalized considering the flexibility of the structure observed during the activation of the solid, which might also be evidenced by the change of slope observed in the low-pressure range of the N_2 sorption isotherm (Fig. S10). In comparison with the non-functionalized version (MIL-47(V)),[36] MIL-47(V)-$(SCH_3)_2$ presents roughly half of the surface area and pore volume, in line with the presence of the bulky methylthio ($-SCH_3$) groups in the pores.

Eventually, the chemical stability of the materials was also evaluated by suspending a controlled amount of powdered samples (2 mg mL^{-1}) in water and in a variety of industrially relevant organic solvents (*i.e.*, ethanol (EtOH), MeOH, tetrahydrofuran (THF), acetonitrile (ACN), DMF and hexane) under stirring overnight. The structural integrity was then evaluated by PXRD (Fig. S23 and S24 for (DMA)KVO(DSBDC) and MIL-47(V)-$(SCH_3)_2$, respectively). While (DMA)KVO(DSBDC) is stable only in organic solvents and dissolved in water, MIL-47(V)-$(SCH_3)_2$ retained its structure under all tested conditions. Here again, the flexibility of MIL-47(V)-$(SCH_3)_2$ was evidenced by the changes observed in the PXRD pattern upon immersion in DMF, which reverted to the pristine PXRD pattern after solvent exchange.

Optical characterization

The optoelectronic properties of both materials, as well as the free ligand H_4DSBDC, were evaluated using diffuse reflectance (DR) UV-Vis spectroscopy in the 200–800 nm range (Fig. 3 and Fig. S25). The H_4DBSDC ligand exhibits low reflectance (hence high absorbance), from 200 to ~450 nm, likely associated with π–π* transitions. Both MOFs also absorb light in the visible range, but with different features. For MIL-47(V)-$(SCH_3)_2$, light is absorbed from 200 up to 550 nm; this can be associated with the ligand-centered π–π* transition (see above) together with additional V^{III} centered d–d transitions. These features

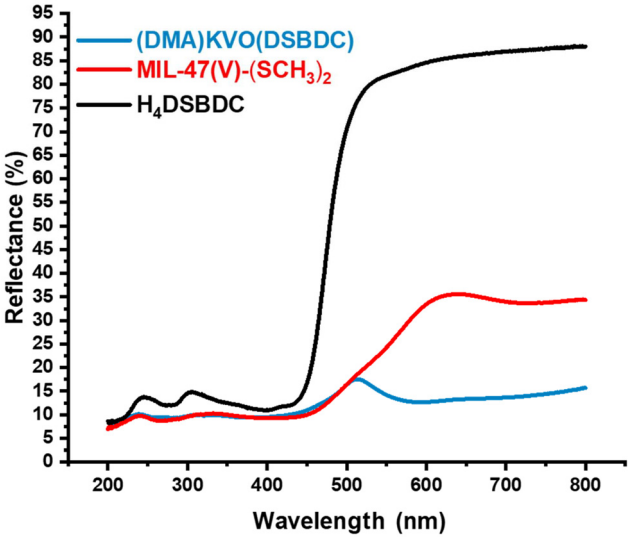

Fig. 3 DR-UV-Vis spectra of (DMA)KVO(DSBDC) (blue), MIL-47(V)-$(SCH_3)_2$ (red) and the H_4DSBDC ligand (black).

are also found for (DMA)KVO(DSBDC), but an additional broad band spanning from ~550 to at least 800 nm is also visible. This last band is likely associated with LMCT, similarly to what is found in analogous vanadium-phenolate complexes,[45,50] but here through V–S bonds. The optical band gaps were estimated using Tauc plots, reaching 2.19 and 2.43 eV for MIL-47(V)-$(SCH_3)_2$ and (DMA)KVO(DSBDC), respectively (Fig. S27 and S26). These values should nevertheless be considered with caution, knowing that the reflectance spectra involve multiple contributions, as discussed above. In addition, photoluminescence (PL) experiments were conducted using an excitation wavelength of 415 nm (Fig. S28), revealing that both materials exhibit an emission band at 510 nm, possibly with a slightly lower intensity for MIL-47(V)-$(SCH_3)_2$.

Photocatalytic desulfurization

Considering their chemical stability and strong light absorption in the visible range, (DMA)KVO(DSBDC) and MIL-47(V)-$(SCH_3)_2$ were evaluated as photocatalysts for the PODS of DBT, using H_2O_2 as an oxidant and visible light as the energy source (Table 3). The evolution of the amounts of both DBT and its oxidation product DBT sulfone (Scheme S1) was followed by high-performance liquid chromatography (HPLC). As the reaction could not be carried out directly in oil due to the poor dispersion of the MOF in this apolar medium and extraction issues, initial tests were conducted in a liquid–solid phase system based on ACN, in which the MOFs are stable (see above) and easily dispersed. This allowed comparing the visible-light-driven photocatalytic activity of both materials while minimizing the mass-transfer limitations encountered in a liquid–liquid–solid phase system (L(ACN)–L(oil)–S(catalyst), see below). A reaction time of 3 h was selected, in line with previous studies on V-based MOFs for thermally driven

Table 3 DBT removal and yield of DBT sulfone using V-MOF photocatalysts

Entry	Photocatalyst	H_2O_2/DBT molar ratio	Irradiation	Removal of DBT[d] (%)	Yield of DBT sulfone[d] (%)
1	—	3	Yes	—	—
2	—	6	Yes	—	—
3	MIL-47(V)-$(SCH_3)_2$ [a]	—	No	—	—
4	MIL-47(V)-$(SCH_3)_2$ [b]	3	No	16 ± 1	7.2 ± 0.9
5	MIL-47(V)-$(SCH_3)_2$ [c]	3	Yes	24 ± 1	15 ± 2
6	MIL-47(V)-$(SCH_3)_2$ [c]	6	Yes	42 ± 1	40 ± 1
7	(DMA)KVO(DSBDC)[c]	3	Yes	20 ± 1	13 ± 1
8	(DMA)KVO(DSBDC)[c]	6	Yes	44 ± 3	38 ± 2

[a] Reaction conditions: 20 mg of photocatalyst, 10 mL of a solution of 575 ppm DBT in ACN, in darkness and in the absence of H_2O_2 for 3 h. [b] Reaction conditions: 20 mg of photocatalyst, 10 mL of a solution of 575 ppm DBT in ACN, in darkness for 3 h. [c] Reaction conditions: 20 mg of photocatalyst, 10 mL of a solution of 575 ppm DBT in ACN, under visible light irradiation for 3 h. [d] DBT removal and yield of DBT sulfone determined by HPLC.

ODS.[54] Control experiments performed in the absence of the MOF photocatalyst and with various amounts of H_2O_2 (H_2O_2/DBT molar ratios = 3 and 6, entries 1 and 2, respectively) resulted in negligible DBT removal. Furthermore, adsorption and oxidation tests using MIL-47(V)-$(SCH_3)_2$ in the dark (entries 3 and 4) revealed the limited DBT adsorption capacity of the material, and only a minor amount of the oxidation product (7.2 ± 0.9%). In the absence of a photocatalyst and under dark conditions, only DBT extraction into the polar phase was observed (blank P, Fig. 4a), with a DBT removal of 44 ± 3%, and no DBT sulfone was detected in the ACN phase. A blank thermal experiment at room temperature without a photocatalyst resulted in only DBT extraction, with no sulfone formation (blank TC, Fig. 4b).

In contrast, under visible light, both MIL-47(V)-$(SCH_3)_2$ and (DMA)KVO(DSBDC) displayed significant DBT removal (*i.e.*, 23.8 ± 1.1% and 20.2 ± 1.0%, respectively) using an H_2O_2/DBT molar ratio of 3 (entries 5 and 7). When doubling the amount of the oxidant (H_2O_2/DBT = 6), the removal of DBT increased further, reaching 41.8 ± 1.4% and 44.5 ± 2.6% for MIL-47(V)-$(SCH_3)_2$ and (DMA)KVO(DSBDC), respectively (entries 6 and 8), indicating a positive correlation between the concentration of the oxidant and the photocatalytic performance. Note that both materials exhibited comparable photocatalytic activity after 3 h, suggesting that the additional LMCT visible-light absorption path in (DMA)KVO(DSBDC) does not play a significant role in the photocatalytic process.

Furthermore, the structural integrity of both photocatalysts after the reaction was evaluated by PXRD (Fig. S29 and S30). Both MOFs retained their crystallinity at low oxidant concentration (H_2O_2/DBT = 3). However, at high oxidant concentration (H_2O_2/DBT = 6), a broadening of the diffraction peaks was observed for (DMA)KVO(DSBDC), suggesting a partial degradation.

Kinetic studies for both V-based photocatalysts were performed under optimized conditions (*i.e.*, H_2O_2/DBT molar ratio = 6). As can be seen in Fig. S31, DBT removals of 43 ± 2% and 41 ± 2% were achieved within 30 min for MIL-47(V)-$(SCH_3)_2$ and (DMA)KVO(DSBDC), respectively, corresponding to DBT sulfone yields of 39 ± 1% and 37 ± 2%. Notably, MIL-47

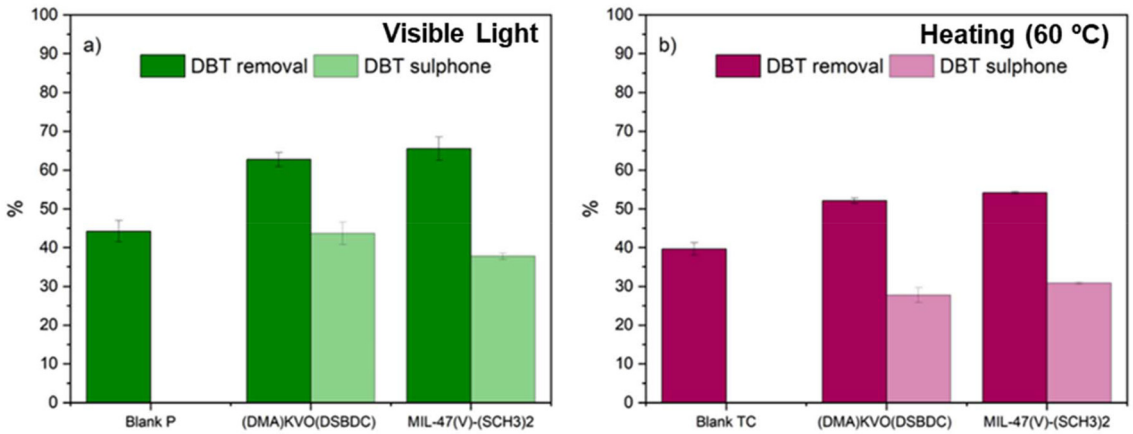

Fig. 4 Comparison of the (a) photocatalytic (P) and (b) thermal catalytic (TC) performance of (DMA)KVO(DSBDC) and MIL-47(V)-$(SCH_3)_2$ in terms of DBT removal efficiency and DBT sulfone yield. Reaction conditions: 20 mg of catalyst, 10 mL of a solution of 575 ppm DBT in *n*-octane, 5 mL of ACN, 20 μL of a solution of 30% H_2O_2 and 3 h of visible light irradiation (photocatalysis) or 60 °C for 3 h (thermal catalysis). Blank experiments, reaction conditions: 10 mL of a solution of 575 ppm DBT in *n*-octane, 5 mL of ACN, 20 μL of a solution of 30% H_2O_2 under dark conditions (blank P) and at room temperature (blank TC).

(V)-$(SCH_3)_2$ reached a DBT sulfone yield of 40 ± 2 after just 15 min, significantly higher than that of (DMA)KVO(DSBDC) (27 ± 1.1% in 15 min), indicating a faster DBT oxidation rate for MIL-47(V)-$(SCH_3)_2$ compared to (DMA)KVO(DSBDC). This enhanced oxidative performance is likely not related to the microporosity of MIL-47(V)-$(SCH_3)_2$ (pore size does not favor fast DBT diffusion), but rather results from its higher external surface exposed to DBT, arising from the smaller particle size and possibly a lower recombination rate of photogenerated electron–hole pairs, as suggested by the photoluminescence (PL) analysis.

To evaluate the photocatalytic performance of the V-based MOFs under conditions closer to practical applications, experiments were conducted in a liquid–liquid–solid phase system (L(ACN)–L(oil)–S(catalyst)), using a mixture of 10 mL of a model oil (a solution of DBT in *n*-octane) and 5 mL of ACN, in the presence of H_2O_2 as an oxidant (H_2O_2/DBT molar ratio = 6), under visible light irradiation for 3 h (Fig. 4a). In the absence of a photocatalyst, only extraction of DBT into the polar phase was observed (blank P, Fig. 4a) with a DBT removal of 44 ± 3%, and no DBT sulfone was detected in this phase. Upon addition of the photocatalyst, DBT removal efficiencies of 66 ± 3% and 63 ± 2% were achieved for MIL-47(V)-$(SCH_3)_2$ and (DMA)KVO(DSBDC), respectively. Analysis of the acetonitrile phase confirmed the oxidation of DBT into DBT sulfone, with yields of *ca.* 40% for both materials, suggesting comparable photocatalytic activities under the tested conditions.

Additionally, thermal-driven ODS experiments were also performed to investigate the influence of the energy source (Fig. 4b). Based on previously reported studies on V-MOFs used for thermal-driven ODS,[55,56] the temperature was set at 60 °C. A blank thermal experiment was carried out at room temperature in the absence of a catalyst, resulting in only DBT extraction, with no sulfone formation (blank TC, Fig. 4b). In contrast, in the presence of the catalyst, similar DBT removal efficiencies were obtained for both MOFs (54.2 ± 0.3% and 52.1 ± 0.7% for MIL-47(V)-$(SCH_3)_2$ and (DMA)KVO(DSBDC), respectively). However, the corresponding DBT sulfone yields were lower (30.9 ± 0.3% and 27.8 ± 1.9%) than those obtained under visible light irradiation, indicating that visible-light activation enhances the oxidative performance of both catalysts compared to purely thermal conditions.

The chemical stability of both V-based catalysts was evaluated by PXRD and ICP-MS after 3 and 6 h of reaction. While the PXRD pattern of MIL-47(V)-$(SCH_3)_2$ does not significantly evolve (Fig. S33), that of (DMA)KVO(DSBDC) is significantly modified, with new diffraction peaks appearing after 6 h of reaction (Fig. S32). ICP-MS analysis further revealed a significant leaching of vanadium for this material (7.3 ± 0.4% and 47.3 ± 0.6% after 3 and 6 h of reaction, respectively), while the loss is negligible for MIL-47(V)-$(SCH_3)_2$ (2.7 ± 0.5% and 2.6 ± 0.9% after 3 and 6 h of reaction, respectively), confirming its superior chemical stability. Based on these results, MIL-47(V)-$(SCH_3)_2$ was selected as the best photocatalyst for further analyses. The effect of light exposure time and oxidant concentration was subsequently investigated. The DBT removal efficiency of MIL-47(V)-$(SCH_3)_2$ increased with reaction time, from 57 ± 2% at 30 min to 66 ± 3% at 3 h (see Fig. S34). When the reaction time was fixed at 60 min and the oxidant concentration was doubled (H_2O_2/DBT molar ratio = 12), DBT removal improved significantly (61 ± 2% *vs.* 72.7 ± 0.1%, respectively). Thus, the highest DBT removal efficiency (72.7 ± 0.1%) was achieved at an H_2O_2/DBT molar ratio of 12 and a reaction time of 60 min.

Comparison with other reported MOF-based photocatalysts shows that MIL-47(V)-$(SCH_3)_2$ competes with best behaving materials (Table 4) without the addition of any co-catalyst.

Furthermore, when compared with other V-based MOF catalysts used in thermal-driven ODS, MIL-47(V)-$(SCH_3)_2$ demonstrated improved DBT removal efficiency. The mesoporous vanadium(III) trimesate MIL-100(V) indeed showed 72% DBT removal at 60 °C for 2 h when using H_2O_2 (O/S ratio = 8) as the oxidant.[55] The pristine MIL-47(V) achieved 34.8% DBT removal at 120 °C for 3 h[54] and 55% at 60 °C for 2 h[58] when using oxygen and *tert*-butyl hydroperoxide (TBHP) as oxidants, respectively, suggesting that the SCH_3 functionalization has a positive impact on the activity of MIL-47(V). Overall, these comparisons highlight the efficiency of MIL-47(V)-$(SCH_3)_2$ under visible-light-driven conditions, offering a more sustainable and energy-efficient alternative compared to conventional thermal-driven ODS processes.

Table 4 Performance comparison between different MOFs and MOF-based composites in PODS

Material	Mass of catalyst (mg)/ volume or reaction (mL)	Oxidant/DBT molar ratio	DBT concentration (ppm)	Time (min)	Temperature (°C)	Removal (%)	Ref.
MIL-47(V)-$(SCH_3)_2$	20/10	12[a]	575	60	RT	73	This work
HKUST-1	10/n.a.	10[a]	100	20	RT	39	8
$BiVO_4$@HKUST-1	10/n.a.	10[a]	100	20	RT	55	8
ZIF-67	80/80	8[a]	500	60	30	65	11
MIL-125-NH_2	10/7	5[a,b]	1000	25	30	35	13
MIL-101(Fe)	90/180	3[a]	500	30	RT	45	57
0.133CeO_2/MIL-101(Fe)	90/180	3[a]	500	30	RT	45	57
UiO-66-NH_2	20/50	—[b]	250	90	RT	25	12
Ce-UiO-66-NH_2	20/50	—[b]	250	90	RT	35	12

n.a.: not available. [a] H_2O_2. [b] O_2.

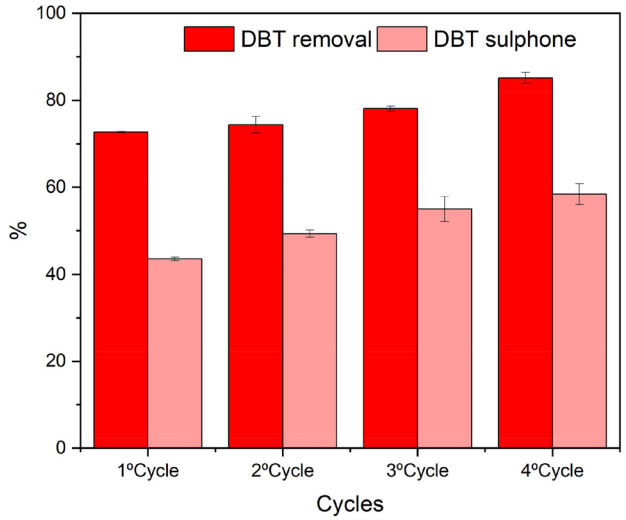

Fig. 5 DBT removal efficiency and DBT sulfone yield across consecutive 60 min photocatalytic cycles using MIL-47(V)-$(SCH_3)_2$.

Finally, the reusability of MIL-47(V)-$(SCH_3)_2$ was evaluated under the optimized reaction conditions. 4 successive cycles were carried out. As shown in Fig. 5, a good cyclability of the photocatalyst was observed, with DBT removal efficiencies exceeding 70% during the first 3 cycles, followed by a further increase during the 4th cycle (85 ± 1%). The stability of the MOF was then evaluated by PXRD (Fig. S35), FTIR (Fig. S36), ICP-MS (Table S6) and morphological analysis (Fig. S37). As can be seen in Fig. S35, although the diffraction peaks corresponding to the MOF structure were retained, a broadening is observed after the 4th cycle, suggesting a partial degradation of MIL-47(V)-$(SCH_3)_2$ upon extended use. This was further confirmed by FTIR (Fig. S36), which revealed the appearance of new bands at 1700 and 1143 cm^{-1}, associated with free carboxylic groups and possibly S=O bonds, respectively, and thus suggesting a partial degradation of the framework and oxidation of the ligand. Finally, ICP-MS (Table S6) revealed only a slight, but continuous, release of vanadium (from 3.9% to 10.7% in the 1st and 4th cycle, respectively). Hence, the enhanced activity observed during the last cycle may be related to an increase in exposed vanadium sites as a consequence of the ligand leaching and oxidation and consequently partial amorphization of the MOF particles.

Conclusions

Two novel V-based MOFs were successfully synthesized and comprehensively characterized. Both materials are constructed from the DSBDC ligand, which displayed distinct coordination modes depending on the synthetic conditions. The addition of a base afforded (DMA)KVO(DSBDC), in which the ligand binds to V(IV) through both S and O atoms, while the use of a DMF/MeOH mixture promoted the formation of the porous MIL-47(V)-$(SCH_3)_2$, a functionalized analogue of MIL-47(V) containing –SCH_3 functional groups derived from an *in situ* condensation reaction. Both materials presented good chemical stability in various organic solvents, which, combined with their ability to absorb light in the visible range, makes them suitable candidates as photocatalysts for the PODS reaction, reaching ~60% DBT removal in the L–L–S system. Among them, MIL-47(V)-$(SCH_3)_2$ showed superior performance and chemical stability compared to (DMA)KVO(DSBDC). Upon optimization of the reaction conditions, MIL-47(V)-$(SCH_3)_2$ achieved 72% DBT removal, maintaining its activity for 4 cycles. These results pave the way for the development of new V-based photocatalysts for PODS, provided that their long-term stability can be improved.

Experimental methods

Synthetic procedures

All the chemicals were purchased from Merck–Sigma Aldrich and used as received without further purification: VCl_3 (97%, 157.3 g mol^{-1}), VO(acac) (98%, 265.16 g mol^{-1}), KOH (85%, 56.11 g mol^{-1}), DMF (ACS reagent, ≥99.8%), and MeOH (ACS reagent, ≥99.8%). H_4DSBDC was synthesized using the reported procedure.[31]

Synthesis of (DMA)KVO(DSBDC) or (C_2H_8N)KVO($C_8H_2O_4S_2$) (MW = 378.35 g mol^{-1}). In a 23 mL Teflon-lined autoclave reactor, 115.08 mg of H_4DSBDC (0.5 mmol) and 78.6 mg of VCl_3 (0.5 mmol) were dissolved in 9 mL of DMF. Then, 1 mL of a 1 M KOH aqueous solution was added dropwise. The mixture was heated at 180 °C for 16 h. The obtained dark green crystals were recovered by filtration, washed with DMF, H_2O and EtOH and dried in air (~140 mg recovered).

For the solid prepared using $VO(acac)_2$, the same procedure was followed, adding 132.5 mg of $VO(acac)_2$ (0.5 mmol) instead of VCl_3.

Synthesis of MIL-47(V)-$(SCH_3)_2$ or $V^{III}OH(C_{10}H_8O_4S_2)$ (MW dry = 324.24 g mol^{-1}). In a 16 mL Teflon-lined autoclave reactor, 476.4 mg of H_4DSBDC (2.07 mmol) and 217.1 mg of VCl_3 (1.38 mmol) were dissolved in 7.36 mL of DMF and 1.84 mL of MeOH. The mixture was heated at 180 °C for 50 h. The obtained pale brown powder was recovered by filtration, washed with DMF and MeOH and dried in air (~480 mg recovered).

For the solid prepared using acetic acid, the same procedure was followed, adding 0.286 mL of AcOH (5 mmol, H^+/M ratio = 10) after the addition of the solvents.

Activation of MIL-47(V)-$(SCH_3)_2$. 200 mg of the solid was suspended in 5 mL of MeOH under stirring. After 2 h, the solid was recovered by centrifugation and dried in air.

Crystallographic studies

SC-XRD data from (DMA)KVO(DSBDC) were collected at room temperature using a Rigaku XtaLAB Synergy diffractometer working with Mo Kα radiation. The CrysAlisPro suite was used to integrate and scale intensities, and a semi-empirical absorp-

tion correction (ABSPACK) was applied on the basis of multiple scans of equivalent reflections. The structure was solved by using SHELXT[59] and refined with the full matrix least squares routine SHELXL.[60] Non-H-atoms were refined anisotropically. H atoms were placed in calculated positions and refined with idealized geometries.

The MIL-47(V)-$(SCH_3)_2$ structure was elucidated from powder X-ray diffraction (PXRD) data collected on the CRISTAL beamline at Synchrotron SOLEIL (L'Orme des Merisiers, France). A monochromatic beam was extracted from the U20 undulator beam by means of a Si(111) double monochromator. Its wavelength of 0.671415 Å was refined from a LaB_6 (NIST Standard Reference Material 660a) powder diagram recorded prior to the experiment. The sample was loaded in a 0.7 mm capillary (Borokapillaren, GLAS, Schönwalde, Germany) mounted on a spinner rotating at about 5 Hz to improve the particles' statistics. Diffraction data were collected in continuous scanning mode with a MYTHEN2 X 9K detector (Dectris), allowing measurement in less than 5 minutes. Structural investigations were performed using the TOPAS (indexing, simulated annealing, difference Fourier calculations and Rietveld refinement) and EXPO (whole powder pattern decomposition and direct methods calculations) programs.[59,60] The LSI-indexing method converged unambiguously to a monoclinic unit cell with M_{20} = 87 (see Table 1). Systematic extinctions were consistent with the $C2/c$ space group, which was used to initialize the structural determination. Direct methods led us to locate the vanadium atom on a symmetry center. The organic ligand also localized on a symmetry center was then treated as a rigid body, and its orientation was allowed to vary during a simulated annealing process. The guest DMF was located by both difference Fourier calculations and the simulated annealing process. The final Rietveld plot (Fig. S7) corresponds to satisfactory model indicators and profile factors (see Table S2). This involves 24 structural parameters: 1 scale factor, 1 atomic coordinate for the O3 atom, 9 parameters for the orientation and the translation of the organic moieties, 5 distances and 4 angles inside the organic ligand, 3 temperature factors and 1 occupancy factor for the DMF molecule.

CCDC 2246050 and 2497420 contain the supplementary crystallographic data for (DMA)KVO(DSBDC) and MIL-47(V)-$(SCH_3)_2$.

Physicochemical characterization

PXRD patterns were collected either in Bragg–Brentano mode with a Bruker D8 Advance diffractometer or in Debye–Scherrer mode with an INEL XRG3500 diffractometer, both equipped with a Cu anode (λ = 1.5406 Å).

Thermodiffraction experiments were carried out in an Anton Paar XRK 900 high-temperature chamber with the Bruker D8 Advance diffractometer. TGA were conducted under air at 5 °C min^{-1} up to 800 °C on Setaram SENSYSevo equipment. For the ICP-AES experiments, solids were first dissolved in 20% w/w HNO_3 and further analyzed using an iCAP 6300 radial analyser (Thermo Scientific). Inductively coupled plasma mass spectrometry (ICP-MS) experiments were performed on a Perkin SCIEX NexION 300D at Servicios Centrales de Apoyo a la Investigación (SCAI), University of Málaga. Prior to the analysis, the samples were dehydrated and then digested in a HNO_3 solution (20% w/w) at 60 °C. Elemental analyses were carried out in a Flash 2000 analyzer from Thermo Scientific. N_2 sorption experiments were carried out in Micromeritics 3Flex equipment. The samples were degassed at 150 °C for 16 h under secondary vacuum prior to their analysis. Scanning electron microscopy (SEM) was carried out on a JEOL JSM-5800LV microscope. Samples were pasted on carbon tape and further coated with carbon to improve the surface electronic conductivity. Optical microscopy images were acquired using a Zeiss SteREO Discovery V20 microscope equipped with a Zeiss Axiocam 208 color digital camera.

Fourier transform infrared (FTIR) spectra were recorded at room temperature with a Bruker alpha FTIR spectrometer in the attenuated total reflectance (ATR) mode between 400 and 4000 cm^{-1}. Diffuse reflectance UV-Vis spectra were collected in a PerkinElmer Lambda 1050 equipped with an integrating sphere module. Photoluminescence spectra were acquired in an FS5 fluorescence spectrophotometer (Edinburgh Instruments) using a Xe lamp, exciting at 415 nm (4 slits).

Photocatalytic desulfurization experiments

The visible-light-driven ODS reactions were carried out in a 20 mL glass reactor. In a typical liquid–solid (L(ACN)–S(catalyst)) system experiment, 20 mg of photocatalyst, 10 mL of a 575 ppm DBT solution in ACN and 10 or 20 μL of a solution of 30% H_2O_2 (0.097 or 0.194 mmol) were added to the flask. The resulting dispersion was stirred at 900 rpm and exposed to visible light irradiation (using a 300 W Xe lamp at $\lambda > 400$ nm). After 3 h, the photocatalyst was separated by centrifugation, and the supernatant was analyzed using high-performance liquid chromatography (HPLC) (Jasco LC-4000 series system, equipped with a photodiode array detector (PDA) MD-4015, C18 column 5 μm, 4.6 × 250 mm). The mobile phase consisted of a mixture of 90 : 10 ACN : H_2O, with a flow rate of 0.8 mL min^{-1}.

For the liquid–liquid–solid (L(ACN)–L(oil)–S(catalyst)) system, the reaction was performed in a biphasic mixture composed of 10 mL of a 575 ppm DBT solution in *n*-octane and 5 mL of ACN as the extracting solvent, in the presence of 20 mg of photocatalyst and 20 or 40 μL of 30% H_2O_2 (0.194 or 0.388 mmol). The oil phase was analyzed by gas chromatography (GC) (Agilent GC 8860, equipped with a FID detector, an HP-PLOT 5A column, 30 m, 0.53 mm, 25 μm). The injector and detector temperatures were set at 290 and 310 °C, respectively. The column temperature was maintained at 80 °C for 1 min, then increased to 200 °C at a ramp rate of 15 °C min^{-1} and held at 200 °C for 10 min.

For recycling experiments, the photocatalyst was separated by centrifugation, washed with ACN and dried at 100 °C for 2 h. Then, the photocatalyst was placed in contact with a fresh DBT solution under identical conditions.

Conflicts of interest

There are no conflicts to declare.

Data availability

The data that support the findings of this study are available from the corresponding authors, Pablo Salcedo-Abraira, Yolanda Pérez and Thomas Devic, upon reasonable request.

Supplementary information (SI) is available. See DOI: https://doi.org/10.1039/d5qi02257f.

CCDC 2246050 and 2497420 contain the supplementary crystallographic data for this paper.[61a,b]

Acknowledgements

The authors acknowledge the Agence Nationale de la Recherche for the funding of the project 'ThioMOFs' (grant ANR-19-CE08-0029-01 and -03) and the NAPOLION project (PID2022-139956OB-I00) funded by MICIU/AEI /10.13039/501100011033 and by FEDER, UE. Synchrotron SOLEIL is thanked for providing access to the CRISTAL beamline, and Erik Elkaïm for the PXRD data collection. The ICP-AES analyses were performed at the LPG-UMR 6112, Nantes Université (C. La, M. Rivoal), which is also thanked. P. S.-A. is thankful for Grant JDC2022-048964-I, funded by MICIU/AEI/10.13039/501100011033 and by the "European Union NextGenerationEU/PRTR". For the purpose of Open Access, a CC-BY public copyright licence has been applied by the authors to the present document and will be applied to all subsequent versions up to the Author Accepted Manuscript arising from this submission. Funding for the open access charge was provided by Universidad de Granada.

References

1) New WHO Global Air Quality Guidelines aim to save millions of lives from air pollution. https://www.who.int/news/item/22-09-2021-new-who-global-air-quality-guidelines-aim-to-save-millions-of-lives-from-air-pollution (accessed 2025-09-04).

2 P. Orellano, J. Reynoso and N. Quaranta, Short-Term Exposure to Sulphur Dioxide (SO2) and All-Cause and Respiratory Mortality: A Systematic Review and Meta-Analysis, *Environ. Int.*, 2021, **150**, 106434, DOI: 10.1016/j.envint.2021.106434.

3 B. Saha, S. Vedachalam and A. K. Dalai, Review on Recent Advances in Adsorptive Desulfurization, *Fuel Process. Technol.*, 2021, **214**, 106685, DOI: 10.1016/j.fuproc.2020.106685.

4 A. Haruna, Z. M. A. Merican and S. G. Musa, Recent Advances in Catalytic Oxidative Desulfurization of Fuel Oil – A Review, *J. Ind. Eng. Chem.*, 2022, **112**, 20–36, DOI: 10.1016/j.jiec.2022.05.023.

5 C. Peng, R. Guo, X. Feng and X. Fang, Tailoring the Structure of Co-Mo/Mesoporous γ-Al_2O_3 Catalysts by Adding Multi-Hydroxyl Compound: A 3000 Kt/a Industrial-Scale Diesel Ultra-Deep Hydrodesulfurization Study, *Chem. Eng. J.*, 2019, **377**, 119706, DOI: 10.1016/j.cej.2018.08.092.

6 I. Shafiq, S. Shafique, P. Akhter, M. Ishaq, W. Yang and M. Hussain, Recent Breakthroughs in Deep Aerobic Oxidative Desulfurization of Petroleum Refinery Products, *J. Cleaner Prod.*, 2021, **294**, 125731, DOI: 10.1016/j.jclepro.2020.125731.

7 C. Wang, A.-R. Li and Y.-L. Ma, Phosphomolybdic Acid Niched in the Metal-Organic Framework UiO-66 with Defects: An Efficient and Stable Catalyst for Oxidative Desulfurization, *Fuel Process. Technol.*, 2021, **212**, 106629, DOI: 10.1016/j.fuproc.2020.106629.

8 A. Raeisi, A. N. Chermahini and M. M. Momeni, A Novel Photocatalytic and Photoelectrocatalytic System for Oxidative Desulfurization of Model Fuel Using BiVO4@HKUST-1 Composite in Powder and Deposited on Fluorine-Doped Tin Oxide, *J. Photochem. Photobiol., A*, 2022, **433**, 114190, DOI: 10.1016/j.jphotochem.2022.114190.

9 S. Salehian, A. Larimi, A. A. Asgharinezhad, N. Khallaghi, T. N. Borhani and C. Ghotbi, Magnetic Z-Scheme Bismuth Molybdate(1-x)/Fe3O4@MIL-125(Ti)(x) Nanocomposite as a High-Performance Visible-Light-Active Photocatalyst for Ultra-Deep Oxidative Desulfurization of Liquid Fuel, *Surf. Interfaces*, 2023, **42**, 103432, DOI: 10.1016/j.surfin.2023.103432.

10 M. Beshtar, A. Larimi, A. A. Asgharinezhad and F. Khorasheh, Ultra-Deep Photocatalytic Oxidative Desulfurization of Model Fuel Using Ti-UiO-66(Zr) Metal–Organic Framework, *Catal. Lett.*, 2024, **154**(6), 2633–2647, DOI: 10.1007/s10562-023-04506-9.

11 S. M. Flihh and S. H. Ammar, Zeolitic Imidazolate Framework Grafted by Cobalt Tungstate as an Efficient Photocatalyst for Photocatalytic Oxidative Desulfurization of Dibenzothiophene, *Mater. Sci. Semicond. Process.*, 2022, **149**, 106894, DOI: 10.1016/j.mssp.2022.106894.

12 H. Fakhri, A. Esrafili, M. Farzadkia, R. Boukherroub, V. Srivastava and M. Sillanpää, Preparation of Tungstophosphoric Acid/Cerium-Doped NH 2 -UiO-66 Z-Scheme Photocatalyst: A New Candidate for Green Photo-Oxidation of Dibenzothiophene and Quinoline Using Molecular Oxygen as the Oxidant, *New J. Chem.*, 2021, **45**(24), 10897–10906, DOI: 10.1039/D1NJ00328C.

13 K. Zhang, F. Chu, Y. Hu, X. Huang, G. Zhao and G. Wang, Ce-Doped MIL-125-NH2 Coupled Ce4+/Ce3+ and Ti4+/Ti3+ Redox Mediators for Thermo-Enhanced Photocatalytic Oxidative Desulfurization, *Chin. Chem. Lett.*, 2023, **34**(5), 107766, DOI: 10.1016/j.cclet.2022.107766.

14 M. Alhaddad, A. Shawky and Z. I. Zaki, Photocatalytic Oxidative Desulfurization of Thiophene by Exploiting a Mesoporous V2O5-ZnO Nanocomposite as an Effective Photocatalyst, *Catalysts*, 2022, **12**(9), 933, DOI: 10.3390/catal12090933.

15 A. S. Belousov and I. Shafiq, Towards the Sustainable Production of Ultra-Low-Sulfur Fuels through Photocatalytic Oxidation, *Catalysts*, 2022, **12**(9), 1036, DOI: 10.3390/catal12091036.

16 Y. Pan, S. Sanati, R. Abazari, A. Jankowska, J. Goscianska, V. Srivastava, U. Lassi and J. Gao, Vanadium- and Manganese-Based Metal-Organic Frameworks for Potential Environmental and Catalysis Applications, *Coord. Chem. Rev.*, 2025, **522**, 216231, DOI: 10.1016/j.ccr.2024.216231.

17 R. G. Pearson, Hard and Soft Acids and Bases, *J. Am. Chem. Soc.*, 1963, **85**(22), 3533–3539, DOI: 10.1021/ja00905a001.

18 L. Sun, T. Miyakai, S. Seki and M. Dincă, Mn 2 (2,5-Disulfhydrylbenzene-1,4-Dicarboxylate): A Microporous Metal–Organic Framework with Infinite (−Mn–S−) ∞ Chains and High Intrinsic Charge Mobility, *J. Am. Chem. Soc.*, 2013, **135**(22), 8185–8188, DOI: 10.1021/ja4037516.

19 L. Sun, C. H. Hendon, M. A. Minier, A. Walsh and M. Dincă, Million-Fold Electrical Conductivity Enhancement in Fe 2 (DEBDC) versus Mn 2 (DEBDC) (E = S, O), *J. Am. Chem. Soc.*, 2015, **137**(19), 6164–6167, DOI: 10.1021/jacs.5b02897.

20 J. He, C. Yang, Z. Xu, M. Zeller, A. D. Hunter and J. Lin, Building Thiol and Metal-Thiolate Functions into Coordination Nets: Clues from a Simple Molecule, *J. Solid State Chem.*, 2009, **182**(7), 1821–1826, DOI: 10.1016/j.jssc.2009.04.024.

21 S. Du, M. Cui and Z. He, Approach toward Iron(II) Coordination Polymers Based on Chain Motifs with Thiolate or Mixed Thiolate/Carboxylate Bridges: Structures and Magnetic Properties, *Inorg. Chem.*, 2021, **60**(24), 19053–19061, DOI: 10.1021/acs.inorgchem.1c02905.

22 J. He, X. Ye, Z. Liu, L. Tang, J. Hu and Z. Xu, Telltale Diamagnetism at 50 K of a Coordination Polymer System, *Mater. Res. Lett.*, 2022, **10**(7), 496–500, DOI: 10.1080/21663831.2022.2057822.

23 K. K. Yee, N. Reimer, J. Liu, S. Y. Cheng, S. M. Yiu, J. Weber, N. Stock and Z. Xu, Effective Mercury Sorption by Thiol-Laced Metal-Organic Frameworks: In Strong Acid and the Vapor Phase, *J. Am. Chem. Soc.*, 2013, **135**(21), 7795–7798, DOI: 10.1021/JA400212K/SUPPL_FILE/JA400212K_SI_001.PDF.

24 A. S. Munn, F. Millange, M. Frigoli, N. Guillou, C. Falaise, V. Stevenson, C. Volkringer, T. Loiseau, G. Cibin and R. I. Walton, Iodine Sequestration by Thiol-Modified MIL-53(Al), *CrystEngComm*, 2016, **18**(41), 8108–8114, DOI: 10.1039/C6CE01842D.

25 M.-Q. Li, Y.-L. Wong, T.-S. Lum, K. S.-Y. Sze-Yin Leung, P. K. S. Lam and Z. Xu, Dense Thiol Arrays for Metal–Organic Frameworks: Boiling Water Stability, Hg Removal beyond 2 Ppb and Facile Crosslinking, *J. Mater. Chem. A*, 2018, **6**(30), 14566–14570, DOI: 10.1039/C8TA04020F.

26 Y.-L. Wong, Y. Diao, J. He, M. Zeller and Z. Xu, A Thiol-Functionalized UiO-67-Type Porous Single Crystal: Filling in the Synthetic Gap, *Inorg. Chem.*, 2019, **58**(2), 1462–1468, DOI: 10.1021/acs.inorgchem.8b03000.

27 S. Cheng, J. Ouyang, M. Li, Y. Diao, J. Yao, F. Li, Y. Lee, H. H. Sung, I. Williams, Z. Xu and Y. Quan, Charge Separation in Metal–Organic Framework Enables Heterogeneous Thiol Catalysis, *Angew. Chem., Int. Ed.*, 2023, **62**(25), e202300993, DOI: 10.1002/anie.202300993.

28 T.-F. Chen, S.-Y. Han, Z.-P. Wang, H. Gao, L.-Y. Wang, Y.-H. Deng, C.-Q. Wan, Y. Tian, Q. Wang, G. Wang and G.-S. Li, Modified UiO-66 Frameworks with Methylthio, Thiol and Sulfonic Acid Function Groups: The Structure and Visible-Light-Driven Photocatalytic Property Study, *Appl. Catal., B*, 2019, **259**, 118047, DOI: 10.1016/j.apcatb.2019.118047.

29 N. Gedikoglu, P. Salcedo-Abraira, L. H. B. Nguyen, N. Guillou, N. Dupré, C. Payen, N. Louvain, L. Stievano, P. Poizot and T. Devic, Fe(iii)-Carboxythiolate Layered Metal–Organic Frameworks with Interest as Active Materials for Rechargeable Alkali-Ion Batteries, *J. Mater. Chem. A*, 2023, **11**(44), 23909–23921, DOI: 10.1039/D3TA05353A.

30 L. H. B. Nguyen, P. Salcedo-Abraira, D. Le Thanh, N. Gedikoglu, N. Guillou, R. Coatleven, P. Poizot, F. Salles, N. Louvain, L. Stievano and T. Devic, A Fe-Thiolate Layered Metal Organic Framework as a High-Performance Electrode Material for Potassium-Ion Batteries, *Chem. Commun.*, 2025, **61**(53), 9614–9617, DOI: 10.1039/D5CC02470F.

31 L. Vial, R. F. Ludlow, J. Leclaire, R. Pérez-Fernandez and S. Otto, Controlling the Biological Effects of Spermine Using a Synthetic Receptor, *J. Am. Chem. Soc.*, 2006, **128**(31), 10253–10257, DOI: 10.1021/ja062536b.

32 N. Stock, High-Throughput Investigations Employing Solvothermal Syntheses, *Microporous Mesoporous Mater.*, 2010, **129**(3), 287–295, DOI: 10.1016/j.micromeso.2009.06.007.

33 K. Barthelet, J. Marrot, G. Férey and D. Riou, VIII(OH){O2C–C6H4–CO2}.(HO2C–C6H4–CO2H)x(DMF)y(H_2O)Z (or MIL-68), a New Vanadocarboxylate with a Large Pore Hybrid Topology : Reticular Synthesis with Infinite Inorganic Building Blocks?, *Chem. Commun.*, 2004, **4**(5), 520–521, DOI: 10.1039/B312589K.

34 Z. Lu, H. G. W. Godfrey, I. da Silva, Y. Cheng, M. Savage, P. Manuel, S. Rudić, A. J. Ramirez-Cuesta, S. Yang and M. Schröder, Direct Observation of Supramolecular Binding of Light Hydrocarbons in Vanadium(III) and(IV) Metal–Organic Framework Materials, *Chem. Sci.*, 2018, **9**(13), 3401–3408, DOI: 10.1039/C8SC00330K.

35 K. Barthelet, K. Adil, F. Millange, C. Serre, D. Riou and G. Férey, Synthesis, Structure Determination and Magnetic Behaviour of the First Porous Hybrid Oxyfluorinated Vanado(III)Carboxylate: MIL-71 or V iii 2 (OH) 2 F 2 {O 2 C-C 6 H_4, *J. Mater. Chem.*, 2003, **13**(9), 2208–2212, DOI: 10.1039/B306852H.

36 K. Barthelet, J. Marrot, D. Riou and G. Férey, A Breathing Hybrid Organic–Inorganic Solid with Very Large Pores and High Magnetic Characteristics, *Angew. Chem., Int. Ed.*, 2002, **41**(2), 281, DOI: 10.1002/1521-3773(20020118)41:2<281::AID–ANIE281>3.0.CO;2–Y.

37 K. Barthelet, D. Riou and G. Férey, [VIII(H_2O)]3O(O2CC6H4CO2)3·(Cl, 9H_2O) (MIL-59): A Rare Example of Vanadocarboxylate with a Magnetically Frustrated Three-Dimensional Hybrid Framework, *Chem. Commun.*, 2002, **2**(14), 1492–1493, DOI: 10.1039/B202749F.

38 F. Carson, J. Su, A. E. Platero-Prats, W. Wan, Y. Yun, L. Samain and X. Zou, Framework Isomerism in Vanadium Metal–Organic Frameworks: MIL-88B(v) and MIL-101(V), *Cryst. Growth Des.*, 2013, **13**(11), 5036–5044, DOI: 10.1021/cg4012058.

39 S. Biswas, S. Couck, M. Grzywa, J. F. M. Denayer, D. Volkmer and P. Van Der Voort, Vanadium Analogues of Nonfunctionalized and Amino–Functionalized MOFs with MIL–101 Topology – Synthesis, Characterization, and Gas Sorption Properties, *Eur. J. Inorg. Chem.*, 2012, (15), 2481–2486, DOI: 10.1002/ejic.201200106.

40 A. Lieb, H. Leclerc, T. Devic, C. Serre, I. Margiolaki, F. Mahjoubi, J. S. Lee, A. Vimont, M. Daturi and J.-S. Chang, MIL-100(V) – A Mesoporous Vanadium Metal Organic Framework with Accessible Metal Sites, *Microporous Mesoporous Mater.*, 2012, **157**, 18–23, DOI: 10.1016/j.micromeso.2011.12.001.

41 K. Barthelet, D. Riou, M. Nogues and G. Férey, Synthesis, Structure, and Magnetic Properties of Two New Vanadocarboxylates with Three-Dimensional Hybrid Frameworks, *Inorg. Chem.*, 2003, **42**(5), 1739–1743, DOI: 10.1021/ic026175m.

42 Y. Liu, K. Leus, M. Grzywa, D. Weinberger, K. Strubbe, H. Vrielinck, R. Van Deun, D. Volkmer, V. Van Speybroeck and P. Van Der Voort, Synthesis, Structural Characterization, and Catalytic Performance of a Vanadium–Based Metal–Organic Framework (COMOC–3), *Eur. J. Inorg. Chem.*, 2012, **2012**(16), 2819–2827, DOI: 10.1002/ejic.201101099.

43 Z. Zhang and M. J. Zaworotko, Template-Directed Synthesis of Metal–Organic Materials, *Chem. Soc. Rev.*, 2014, **43**(16), 5444–5455, DOI: 10.1039/C4CS00075G.

44 R. L. Richards, Vanadium: Inorganic & Coordination ChemistryBased in Part on the Article Vanadium: Inorganic & Coordination Chemistry by Elizabeth M. Page & Sherilyn A. Wass Which Appeared in the Encyclopedia of Inorganic Chemistry, First Edition, in *Encyclopedia of Inorganic and Bioinorganic Chemistry*, John Wiley & Sons, Ltd, Chichester, UK, 2011. DOI: 10.1002/9781119951438.eibc0236.

45 H. Mkhadder, M. Denis, M. Giménez-Marqués, W. Cañón-Mancisidor, B. Humbert, E. Deunf, P. Poizot and T. Devic, A Tris-Oxovanadium Pyrogallate Complex: Synthesis, Structure, and Magnetic and Electronic Properties, *Dalton Trans.*, 2021, **50**(38), 13399–13406, DOI: 10.1039/D1DT01990B.

46 N. E. Brese and M. O'Keeffe, Bond-Valence Parameters for Solids, *Acta Crystallogr., Sect. B:Struct. Sci.*, 1991, **47**(2), 192–197, DOI: 10.1107/S0108768190011041.

47 H. Leclerc, T. Devic, S. Devautour-Vinot, P. Bazin, N. Audebrand, G. Férey, M. Daturi, A. Vimont and G. Clet, Influence of the Oxidation State of the Metal Center on the Flexibility and Adsorption Properties of a Porous Metal Organic Framework: MIL-47(V), *J. Phys. Chem. C*, 2011, **115**(40), 19828–19840, DOI: 10.1021/jp206655y.

48 J. S. Bashkin, J. C. Huffman and G. Christou, A Synthetic Model Approach to the Manganese(III) Acid Phosphatase and Its Iron(III)-Substituted Form, *J. Am. Chem. Soc.*, 1986, **108**(16), 5038–5039, DOI: 10.1021/ja00276a072.

49 N. Duran, W. Clegg, L. Cucurull-Sánchez, R. A. Coxall, H. R. Jiménez, J.-M. Moratal, F. Lloret and P. González-Duarte, Unprecedented Stabilization of Cobalt(II) in a Tetrahedral S 2 O 2 Environment: The Use of a Redox-Noninnocent Ligand, *Inorg. Chem.*, 2000, **39**(21), 4821–4832, DOI: 10.1021/ic000223q.

50 G. B. Karet, S. L. Castro, K. Folting, J. C. Bollinger, R. A. Heintz and G. Christou, Dinuclear, Trinuclear and Mixed-Metal Hexanuclear Aggregates of Vanadium: Crystal Structures and Properties of [NEt4]3[V2Cl9], [PPh4]2[V3OCl4(O2CC6H4SH)5] and [NEt4]4[V2Li4O2Cl4(O2CC6H4S)4] †, *J. Chem. Soc., Dalton Trans.*, 1998, **1**, 67–72, DOI: 10.1039/a705752k.

51 K. Hegetschweiler, T. Keller, M. Baeumle, G. Rihs and W. Schneider, Electrochemical Reduction of Complexes Containing the [Mo3S(S2)3]4+ Core in Aqueous Media and the Structure of Bis(Triethylammonium) Tris(2-Mercaptobenzoato)Tris(.Mu.-Disulfido)(.Mu.3-Thio)-Triangulo-Trimolybdate(IV), *Inorg. Chem.*, 1991, **30**(23), 4342–4347, DOI: 10.1021/ic00023a011.

52 C. Serre, F. Millange, T. Devic, N. Audebrand and W. Van Beek, Synthesis and, Structure Determination of New Open-Framework Chromium Carboxylate MIL-105 or CrIII(OH)·{O2C–C6(CH_3)4–CO2}·nH_2O, *Mater. Res. Bull.*, 2006, **41**(8), 1550–1557, DOI: 10.1016/j.materresbull.2006.01.013.

53 T. Devic, P. Horcajada, C. Serre, F. Salles, G. Maurin, B. Moulin, D. Heurtaux, G. Clet, A. Vimont, J.-M. Grenèche, B. Le Ouay, F. Moreau, E. Magnier, Y. Filinchuk, J. Marrot, J.-C. Lavalley, M. Daturi and G. Férey, Functionalization in Flexible Porous Solids: Effects on the Pore Opening and the Host–Guest Interactions, *J. Am. Chem. Soc.*, 2010, **132**(3), 1127–1136, DOI: 10.1021/ja9092715.

54 X. Li, Y. Gu, H. Chu, G. Ye, W. Zhou, W. Xu and Y. Sun, MFM-300(V) as an Active Heterogeneous Catalyst for Deep Desulfurization of Fuel Oil by Aerobic Oxidation, *Appl. Catal., A*, 2019, **584**, 117152, DOI: 10.1016/j.apcata.2019.117152.

55 I. Ahmed, C.-U. Kim and S. H. Jhung, Carbon-Supported Vanadium Nitride Catalyst, Prepared from Urea-Loaded MIL-100(V) in the Absence of External Ammonia Flow, Having Good Performance in Oxidative Desulfurization, *J. Cleaner Prod.*, 2023, **384**, 135509, DOI: 10.1016/j.jclepro.2022.135509.

56 N. D. McNamara, G. T. Neumann, E. T. Masko, J. A. Urban and J. C. Hicks, Catalytic Performance and Stability of (V) MIL-47 and (Ti) MIL-125 in the Oxidative Desulfurization of Heterocyclic Aromatic Sulfur Compounds, *J. Catal.*, 2013, **305**, 217–226, DOI: 10.1016/j.jcat.2013.05.021.

57 Q. Huo, G. Liu, H. Sun, Y. Fu, Y. Ning, B. Zhang, X. Zhang, J. Gao, J. Miao, X. Zhang and S. Liu, CeO_2-Modified

MIL-101(Fe) for Photocatalysis Extraction Oxidation Desulfurization of Model Oil under Visible Light Irradiation, *Chem. Eng. J.*, 2021, **422**, 130036, DOI: **10.1016/j.cej.2021.130036**.

58 S. Smolders, T. Willhammar, A. Krajnc, K. Sentosun, M. T. Wharmby, K. A. Lomachenko, S. Bals, G. Mali, M. B. J. Roeffaers, D. E. De Vos and B. Bueken, A Titanium (IV)–Based Metal–Organic Framework Featuring Defect–Rich Ti–O Sheets as an Oxidative Desulfurization Catalyst, *Angew. Chem., Int. Ed.*, 2019, **58**(27), 9160–9165, DOI: **10.1002/anie.201904347**.

59 G. M. Sheldrick, SHELXT – Integrated Space-Group and Crystal-Structure Determination, *Acta Crystallogr., Sect. A: Found. Adv.*, 2015, **71**(1), 3–8, DOI: **10.1107/S2053273314026370**.

60 G. M. Sheldrick, Crystal Structure Refinement with SHELXL, *Acta Crystallogr., Sect. C:Struct. Chem.*, 2015, **71**(1), 3–8, DOI: **10.1107/S2053229614024218**.

61 (*a*) CCDC 2246050: Experimental Crystal Structure Determination, 2025, DOI: **10.5517/ccdc.csd.cc2fd679**; (*b*) CCDC 2497420: Experimental Crystal Structure Determination, 2025, DOI: **10.5517/ccdc.csd.cc2ptry7**.

